

PROCEEDINGS OF SPIE

[SPIDigitalLibrary.org/conference-proceedings-of-spie](https://spiedigitallibrary.org/conference-proceedings-of-spie)

X-ray optics simulation and beamline design for the APS upgrade

Xianbo Shi, Ruben Reininger, Ross Harder, Dean Haeffner

Xianbo Shi, Ruben Reininger, Ross Harder, Dean Haeffner, "X-ray optics simulation and beamline design for the APS upgrade," Proc. SPIE 10388, Advances in Computational Methods for X-Ray Optics IV, 103880C (23 August 2017); doi: 10.1117/12.2274571

SPIE.

Event: SPIE Optical Engineering + Applications, 2017, San Diego, California, United States

X-ray optics simulation and beamline design for the APS upgrade

Xianbo Shi^a, Ruben Reininger^a, Ross Harder^a, and Dean Haeffner^a

^aAdvanced Photon Source, Argonne National Laboratory, Argonne, Illinois 60439, USA;

ABSTRACT

The upgrade of the Advanced Photon Source (APS) to a Multi-Bend Achromat (MBA) will increase the brightness of the APS by between two and three orders of magnitude. The APS upgrade (APS-U) project includes a list of feature beamlines that will take full advantage of the new machine. Many of the existing beamlines will be also upgraded to profit from this significant machine enhancement. Optics simulations are essential in the design and optimization of these new and existing beamlines. In this contribution, the simulation tools used and developed at APS, ranging from analytical to numerical methods, are summarized. Three general optical layouts are compared in terms of their coherence control and focusing capabilities. The concept of zoom optics, where two sets of focusing elements (e.g., CRLs and KB mirrors) are used to provide variable beam sizes at a fixed focal plane, is optimized analytically. The effects of figure errors on the vertical spot size and on the local coherence along the vertical direction of the optimized design are investigated.

Keywords: beamline design; X-ray optics simulation; beam coherence; zoom optics;

1. INTRODUCTION

Fourth-generation synchrotron radiation facilities with much lower emittance compared to their predecessors are being built worldwide. The Advanced Photon Source Upgrade (APS-U) project is working to replace the existing storage ring with a Multi-Bend Achromat (MBA) lattice that will increase the brightness and consequently, the coherent flux, by more than two orders of magnitude. To take full advantage of the new MBA lattice, the APS-U project includes eight feature beamlines focusing on coherence related techniques (e.g., coherence diffraction imaging, ptychography, and X-ray photon correlation spectroscopy) and high-energy applications. In addition, several existing beamlines will be upgraded to utilize the improved brightness of the APS-U source and significantly extend their experimental capabilities. Evidently, the optical design of the new and to be upgraded beamlines needs to be carefully simulated to optimize their performance with the new lattice and at the same time specify the requirements of the optical and mechanical components.

Beamline simulation normally starts with the conceptual design by applying simple analytical formulas. With the help of modern technical computing tools, such as Mathematica,¹ the analytical calculation can take into account a Gaussian beam profile, the optics acceptance (e.g., slits, mirror aperture, CRL transmission), as well as the focusing condition using geometric magnification and diffraction formulas.

In order to include a more accurate source profile, take into account optical aberrations, and the effect of non-ideal optics (e.g., mirror roughness and figure errors), dedicated ray-tracing tools, such as *SHADOW*,^{2,3} Ray,^{4,5} McXtrace,⁶ and xrt⁷ need to be used. *HYBRID*⁸ was developed at the APS to combine ray tracing and wavefront propagation. It was implemented into *SHADOWVUI*⁹ and recently in *ShadowOvi*¹⁰ in the OASYS environment.¹¹ *HYBRID* is added when the beam is clipped and/or figure errors on mirrors and gratings are present. Mirror figure errors can be included from either real metrology data or profiles that are constructed by combining cosine components with different weight and spacial frequencies.¹² One suggested software is the DABAM module¹³ in OASYS, which can provide mirror surface profiles from metrology data or scaled profiles with similar manufacture signatures. These ray-tracing tools can provide statistical information on beam intensity, spot size, divergence and energy spectra at any given position along the beamline. Furthermore, they are useful tools to specify the required finish and mechanical stability of the optical components.

Further author information: (Send correspondence to Xianbo Shi)

E-mail: xshi@aps.anl.gov, Telephone: 1-630-252-9676

Advances in Computational Methods for X-Ray Optics IV, edited by Oleg Chubar,
Kawal Sawhney, Proc. of SPIE Vol. 10388, 103880C · © 2017 SPIE
CCC code: 0277-786X/17/\$18 · doi: 10.1117/12.2274571

The experimental techniques based on coherence rely not only on the phase-space information but also on the full knowledge of the mutual coherence of the beam. The mutual coherence function represents the correlation between electromagnetic fields at different positions and time. The propagation of the mutual coherence function is under intensive studies using different approaches. Existing tools and models include the SRW code,^{14,15} the coherent mode decomposition method,¹⁶ comsyl,¹⁷ and the Mutual Optical Intensity (MOI) model.^{18,19} These methods can provide very accurate results, but the computation cost is normally high. The MOI model was originally developed at the Shanghai Synchrotron Radiation Facility (SSRF).¹⁸ The APS and the SSRF recently extended the model to include non-ideal mirrors.¹⁹ The MOI model can provide not only the beam intensity but also the wavefront and the local coherence function at any position along the beamline in a single calculation.

In this contribution, section 2 summarizes the analytical method used in this work. Section 3 compares three optical layouts in terms of their coherence control and focusing capabilities. In section 4, the concept of zoom optics is demonstrated by using different levels of simulation.

2. THE ANALYTICAL METHOD

The analytical method is mainly useful in the conceptual and preliminary design phase of a beamline where we assume ideal optics. It can provide very fast optimization of the beamline layout with reasonable accuracy when optical aberrations (e.g., large demagnification with a spherical mirror) are not present. In this section, we summarize the basic equations and approximations used in the analytical method.

The undulator radiation from a single electron is normally approximated as a 2D symmetric Gaussian beam with the size σ_p and the divergence σ'_p given by²⁰

$$\sigma_p = \frac{\sqrt{2\lambda L_u}}{2\pi}, \quad \sigma'_p = \sqrt{\frac{\lambda}{2L_u}}, \quad (1)$$

where λ is the photon wavelength, L_u is the undulator length. Strictly speaking, the undulator beam is fully coherent transversely but not Gaussian. The emittance of the single-electron undulator radiation is $\sigma_p \sigma'_p \approx \lambda/2\pi$, instead of $\lambda/4\pi$ for a Gaussian laser beam. The electron beam is normally assumed to be Gaussian with the size of $\sigma_{e,x}$ and $\sigma_{e,y}$ and the divergence of $\sigma'_{e,x}$ and $\sigma'_{e,y}$ in the horizontal (x) and vertical (y) directions, respectively. Therefore, the total beam sizes (Σ_x , Σ_y) and divergences (Σ'_x , Σ'_y) are the convolution of the photon and the electron contributions, given by

$$\Sigma_x = \sqrt{\sigma_{e,x}^2 + \sigma_p^2}, \quad \Sigma_y = \sqrt{\sigma_{e,y}^2 + \sigma_p^2}, \quad \Sigma'_x = \sqrt{\sigma'_{e,x}{}^2 + \sigma_p'^2}, \quad \Sigma'_y = \sqrt{\sigma'_{e,y}{}^2 + \sigma_p'^2}, \quad (2)$$

If the undulator center has an offset δ_u from the electron beam waist (defined as 0), the beam sizes at a given position d are

$$\Sigma_x(d) = \sqrt{\sigma_{e,x}^2 + \sigma_p^2 + (d\sigma'_{e,x})^2 + [(d - \delta_u)\sigma'_p]^2}, \quad \Sigma_y(d) = \sqrt{\sigma_{e,y}^2 + \sigma_p^2 + (d\sigma'_{e,y})^2 + [(d - \delta_u)\sigma'_p]^2}. \quad (3)$$

The beam waists are at $d_{w,x}$ and $d_{w,y}$ where $\Sigma_x(d)$ and $\Sigma_y(d)$ in Eq. 3 achieve their minimum values in the horizontal and the vertical directions, respectively. From Eq. 3 one realizes that the beam waists could not overlap and could shift as a function of the photon energy when the insertion device is not located at the center of the straight section. In Eqs. (2) and (3), the effect of the electron beam energy spread is not considered. Apart from the numerical simulation tools (e.g., SRW and *SPECTRA*²¹), an analytical expression can be also used as a universal function to evaluate the angular and spatial distribution of the undulator radiation, which includes effects of the electron emittance and the energy spread.²²

Considering a single optics focusing system, the RMS focal size (S) and divergence (S') in each direction at the focal plane can be estimated by

$$S = \sqrt{S_{geo}^2 + S_{dif}^2 + S_{err}^2}, \quad S_{geo} = \frac{d_{oi}\Sigma_s}{d_{so}}, \quad S_{dif} = \frac{\alpha\lambda d_{oi}}{2.35\Delta}, \quad (4)$$

$$S' = \sqrt{S_{geo}'^2 + S_{dif}'^2 + S_{err}'^2}, \quad S_{geo}' = \frac{d_{so}\Sigma'_s}{d_{oi}}, \quad S_{dif}' = \frac{\alpha\lambda}{2.35\Delta},$$

where Σ_s and Σ'_s are the sigma size and divergence of the source in either the x or y direction as given by Eq. (2), d_{so} and d_{oi} are the source-to-optics and optics-to-image distances, the subscripts *geo*, *dif*, and *err* stand for geometric demagnification, diffraction, and errors, respectively. Δ is the aperture size defined by the optics acceptance with $\alpha=0.88$ for a rectangular aperture and $\alpha=1.22$ for a circular aperture. For a reflective mirror of length L with a grazing angle of θ , the aperture size is

$$\Delta \approx L \sin \theta. \quad (5)$$

One should note that Eq. (4) tends to overestimate the focal spot size. Normally, the diffraction terms S_{dif} and S'_{dif} are only included when the aperture size Δ is smaller than the beam size at the optics position, or the optics is cutting the beam.

The size (S_{err}) and divergence (S'_{err}) broadening due to figure errors and mechanical vibrations need to be considered separately for different types of optics. For a mirror, the surface error effects and its specification need to be discussed in terms of the power spectral density (PSD) function.¹² Ray-tracing and wavefront propagation codes are needed to accurately study mirror figure errors. When the spot size is not diffraction limited the effect of slope errors can be evaluated analytically and are given by

$$S_{err} = 2\sigma_{se}d_{oi}, \quad S'_{err} = 2\sigma_{se}, \quad (6)$$

with σ_{se} is the RMS slope error of the mirror. For the angular vibration of a mirror, σ_{se} needs to be replaced in Eq. (6) by the RMS angular vibration σ_{vib} .

The selection of a single coherent mode is usually achieved by slitting down the beam to the size of the transverse coherence length. Here we define the coherence length based on a phase-space area method. For a Gaussian laser mode with RMS size and angle width of σ and σ' , we have $\sigma\sigma' = \lambda/4\pi$. A rectangular profile of width $\delta = \sqrt{2\pi}\sigma$ has the same area as a Gaussian profile with the same amplitude. Similarly, for the divergence, $\delta' = \sqrt{2\pi}\sigma'$. Therefore, at any beam position, the coherence phase space area is given by $\delta\delta' = \lambda/2$ for the beam with rectangular size and angular profiles. Based on the van Cittert-Zernike theorem,²³ the coherence length at a distance D from an incoherent source is given by

$$L_c = \frac{\lambda}{2\Omega}, \quad (7)$$

where Ω is the angle of the source viewed from that position, $\Omega = \sqrt{2\pi}\Sigma/D$ for a Gaussian source with RMS size Σ and $\Omega = \delta/D$ for a rectangular source profile with width δ .

The transmission (T_{aper}) of a Gaussian beam with a RMS size of σ through an aperture of size Δ is given by the error function,

$$T_{aper} = \text{erf} \left(\frac{\Delta}{2\sqrt{2}\sigma} \right). \quad (8)$$

Δ can be either the aperture size or the mirror acceptance defined by Eq. (5). The mirror reflectivity R can be assumed constant along the mirror length, which can be calculated using the Fresnel formula with the Nevot-Croce factor to include the surface roughness effects.²⁴ For compound refractive lenses (CRL), the absorption of the material needs to be considered. There is no simple analytical formula, but one can use the mathematical integration directly. The transmission of a 1D CRL focusing in the x direction is given by

$$T_{lens} = \frac{1}{\sqrt{2\pi}\sigma} \int_{-\min(D_0, \Delta)/2}^{\min(D_0, \Delta)/2} \exp \left[-\frac{x^2}{2\sigma^2} - N\mu \left(\frac{x^2}{r_0} + d \right) \right] dx, \quad (9)$$

where N is the number of lenses, μ is the attenuation coefficient, r_0 is the apex radius of the parabolic lens, d is the minimum thickness between two interfaces, and D_0 is the lens diameter or the aperture in front of the lens in the x direction.

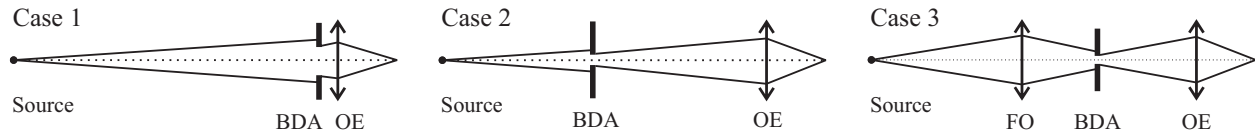


Figure 1. Schematics of three general beamline layouts for beam coherence control and focusing. BDA: beam defining aperture; OE: optical element for focusing; FO: first optics for focusing.

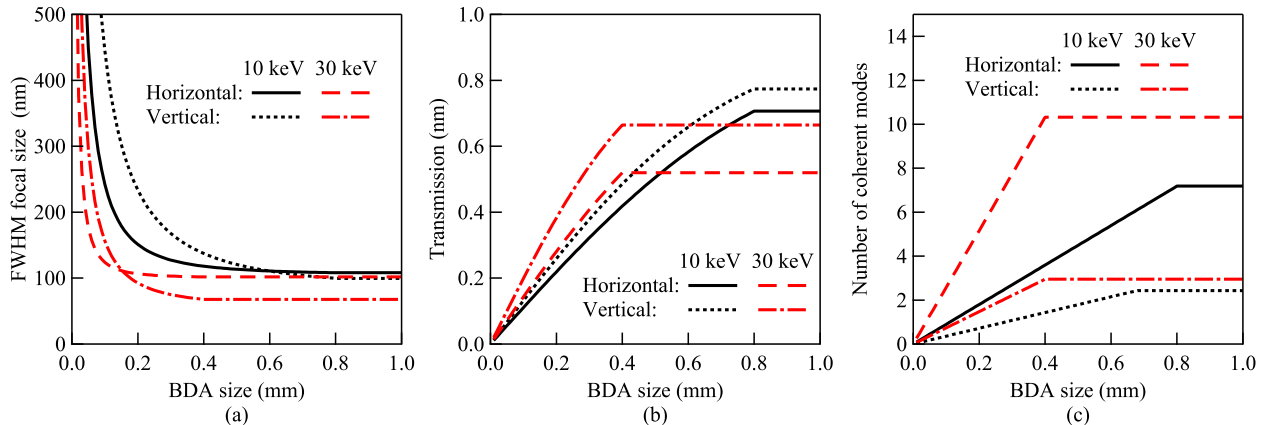


Figure 2. (a) The FWHM focal spot sizes, (b) the total transmission, and (c) the number of coherence modes calculated for case 1 in Fig. 1 with different BDA sizes at 10 keV and 30 keV.

3. ANALYTICAL COMPARISON OF FOCUSING GEOMETRIES

Three general focusing cases (cf. Fig. 1) are compared in terms of controlling beam coherence, focusing capabilities, and the vibration effects from optics using the analytical approach described in section 2. In the calculations, the horizontal and vertical focusing are treated independently. In case 1, the beam coherence is controlled by the beam defining aperture (BDA) in front of the focusing optical element (OE). The OE focuses the source directly to the sample position. In case 2, the BDA controls the coherence and defines the new source which is imaged by the OE. In case 3, the first focusing optics (FO) focuses the source into a secondary source at the BDA position. The BDA controls the coherence and the size of the secondary source. The OE focuses the secondary source to the sample position. To compare the three cases, we consider a beamline with the following parameters: the source is a 4.8 m long undulator with electron beam sizes of $\sigma_x = 14.5 \mu\text{m}$ and $\sigma_y = 2.8 \mu\text{m}$ and divergences of $\sigma'_x = 2.9 \mu\text{rad}$ and $\sigma'_y = 1.5 \mu\text{rad}$; the source-to-sample distance is 70 m; the OE is a KB mirror pair with two 200 mm long mirrors and with 90% reflectivity on each mirror; the working distance between the downstream end of OE and the sample is 100 mm.

Case 1 is studied with different BDA sizes at 10 keV and 30 keV. The mirror grazing angles are 4 mrad and 2 mrad for 10 keV and 30 keV, respectively. In order to match the beam size in both directions, the horizontal mirror is placed downstream of the vertical mirror. The results are shown in Fig. 2. At large BDA sizes, the focal size is determined by the geometric demagnification of the source (Fig. 2a), the transmission is very high (Fig. 2b) but this is at the expense of many coherent modes in the focus (Fig. 2c). When the BDA size is small, the focal spot size is broadened by diffraction, the transmission and the number of coherent modes decrease. The BDA size controls the trade-off between spot size, beam coherence, and flux. Evidently, the transmission and the number of modes reach a maximum when the diffraction is dominated by the mirror size. This occurs at a smaller BDA size for 30 keV than 10 keV since the angle of incidence is smaller at 30 keV.

In practice, the length of the two mirrors can be optimized by maximizing the quantity $T/(S_x S_y)^w$, where T is the total transmission of the focusing system. w is a weighing factor on the focal size taking into account the experimental needs. Fig. 3 shows the above quantity as a function of the length of the two mirrors with $w = 1$ and $w = 2$. The maximum is achieved at ($L_{\text{HKB}} = 155 \text{ mm}$ and $L_{\text{VKB}} = 286 \text{ mm}$) and ($L_{\text{HKB}} = 101 \text{ mm}$ and $L_{\text{VKB}} = 244 \text{ mm}$) for $w = 1$ and $w = 2$, respectively. As seen in this example, $w = 2$ yields a smaller spot size

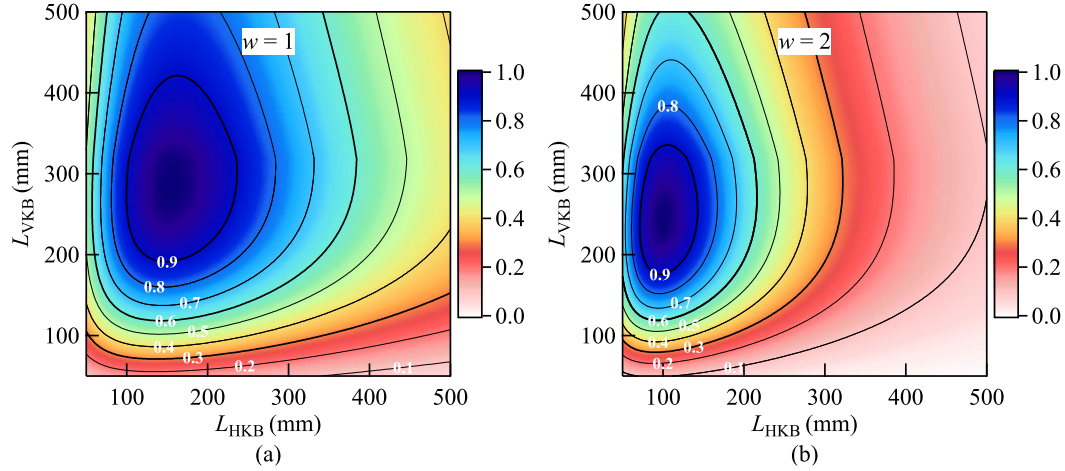


Figure 3. Normalized $T/(S_x S_y)^w$ as a function of the length of the two mirrors with (a) $w = 1$ and (b) $w = 2$. The horizontal mirror (HKB) is downstream of the vertical mirror (VKB).

($89 \times 77 \text{ nm}^2$) and a lower transmission (36%) in comparison with the $w = 1$ case ($98 \times 91 \text{ nm}^2$ and 52%). In most cases, we choose $w = 1$, where the quantity $T/(S_x S_y)$ becomes the flux density.

The disadvantage of the optical design described above (case 1) is that there is no isolation to the vibration from the source and upstream optics (e.g., the monochromator). Considering a double-crystal monochromator (DCM), the relative angular vibration between the two crystals enlarges the virtual source size (Σ_{vir}) as

$$\Sigma_{vir} = \sqrt{\Sigma^2 + (2\sigma_{vib}d_{sm})^2}, \quad (10)$$

where d_{sm} is the source-to-monochromator distance, σ_{vib} here stands for the RMS relative pitch vibration of the DCM. Fig. 4 shows the relative virtual source size broadening (Σ_{vir}/Σ) calculated using Eq. (10) due to the relative pitch vibration of a DCM, diffracting horizontally or vertically, with an RMS value of σ_{vib} . For the horizontal and vertical calculation, we used the 48 bunch mode ($\kappa = 0.99$) with $\Sigma_x = 12.9 \text{ }\mu\text{m}$ and the 324 bunch mode ($\kappa = 0.1$) with $\Sigma_y = 3.6 \text{ }\mu\text{m}$ at 30 keV, which give the smallest source size achievable in each direction with the MBA lattice design.²⁵ As seen in Fig. 4, in order to keep the source size broadening less than 10%, the relative pitch vibration needs to be smaller than 100 nrad and 30 nrad for the horizontal and vertical DCM, respectively. In general, a horizontal monochromator is preferred for the APS-U because of the less stringent stability requirement. We note on passing that a horizontal DCM with a relative pitch vibration $< 25 \text{ nrad}$ RMS over 1-2500 Hz frequency range has been recently demonstrated.²⁶

Case 2 is mostly used at the current APS in the horizontal direction. Since the horizontal beam size of the current APS (as most of the third generation synchrotron facilities) is very big, it is beneficial to use the BDA as the secondary source to achieve small focal spots. For the APS-U, this is no longer the case because of the small source size. Let's consider a BDA located at a source-to-BDA distance of d_{sb} ; and let's neglect the diffraction effects from all optics. In order to achieve smaller focal sizes than in case 1, the BDA size in case 2 should be

$$\Delta < 2.35\Sigma \frac{d_{so} - d_{sb}}{d_{so}}, \quad (11)$$

where d_{so} is the distance between the source and the focusing OE. In other words, the BDA is the preferred source only when Eq. (11) is satisfied. For a 4.8 m long undulator with a resonant energy of 10 keV, the horizontal source sizes calculated using Eq. (2) are $\Sigma_x = 273 \text{ }\mu\text{m}$ and $\Sigma_x = 15.5 \text{ }\mu\text{m}$ for the current APS and the APS-U (324 bunch mode, $\kappa = 0.1$), respectively. Based on Eq. (11) with $d_{so} = 70 \text{ m}$ and $d_{sb} = 25 \text{ m}$, we have $\Delta < 413 \text{ }\mu\text{m}$ and $\Delta < 23.5 \text{ }\mu\text{m}$ for APS and APS-U, respectively. In the existing lattice, the RMS beam size at 25 m is 403 μm , and an aperture of 413 μm accepts 39% of the beam. At APS-U, the RMS beam size at 25 m is 116 μm , and an aperture of 23.5 μm only accepts 8% of the beam. Another argument showing nothing is gained by such aperture in the APS-U is as follows: The coherence length in the horizontal direction of the APS-U at

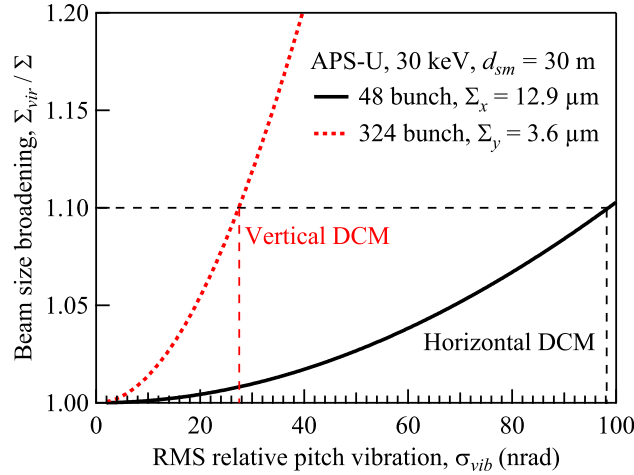


Figure 4. Virtual source size broadening (Σ_{vir}/Σ) as a function of the RMS relative pitch vibration σ_{vib} for a horizontal DCM (solid line) and a vertical DCM (dotted line) at $d_{sm} = 30$ m.

the BDA position calculated by Eq. (7) gives $L_c = 40 \mu\text{m}$. Therefore, the criteria $\Delta < 23.5 \mu\text{m}$ means that the BDA selects less than one coherent mode.

Case 3 is a preferred geometry for APS-U because of the planned low emittance, high stability, high tunability, and high flexibility in beamline optimization. Normally, since the FO position is fixed (e.g., 30 m in the following calculation), the demagnification of the FO can be varied by changing the BDA position. Table 1 compares the calculated results with different BDA sizes for the FO-to-BDA distances of 30 m (FO demagnification factor of 1:1) and 10 m (FO demagnification factor of 3:1). In general, a larger BDA size provides higher flux, but larger focal sizes and lower coherence.

For the FO demagnification of 1:1, the total beamline transmission is dominated by the BDA acceptance. The focal size is dominated by the geometrical demagnification of the BDA size. Thus, the relative flux density almost remains constant.

For the FO demagnification of 3:1, the total transmission is determined by the BDA size as well as the acceptance of the OE (cf. Fig. 1). When the BDA size is smaller than $2L_c$, the focal spot is mainly due to

Table 1. Analytical calculation of the focusing property of case 3 in Fig. 1 with different BDA sizes at 10 keV. All mirrors are 200 mm long with 4 mrad grazing angle.

FO demagnification	1:1				3:1			
$L_{c,H}$ (μm) at BDA	5.3				1.8			
$L_{c,V}$ (μm) at BDA	6.4				2.1			
BDA size H (μm)	$L_{c,H}$	$2L_{c,H}$	$4L_{c,H}$	open	$L_{c,H}$	$2L_{c,H}$	$4L_{c,H}$	open
BDA size V (μm)	$L_{c,V}$	$2L_{c,V}$	$4L_{c,V}$	open	$L_{c,V}$	$2L_{c,V}$	$4L_{c,V}$	open
Focal size H (nm)	111	213	410	732	29	35	52	85
Focal size V (nm)	265	510	621	629	61	76	85	85
Total transmission	3.5%	12%	32%	66%	0.51%	3.8%	14%	32%
Relative flux density*	1	1	1	1.2	2.3	12	26	37
Number of coherent modes	1	4	9.7	18	1	2.8	6.8	12

* The relative flux density is defined as total transmission/focal size H/focal size V, and normalized to the value in the FO demagnification of 1:1 case with a BDA size of $L_{c,H} \times L_{c,V}$ (first column).

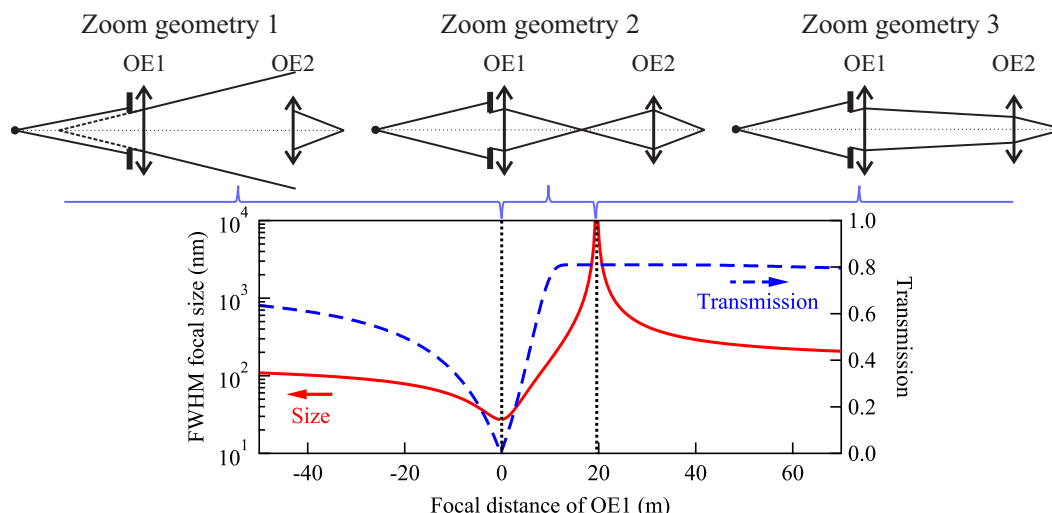


Figure 5. Three zoom geometries and the calculated focal spot sizes (solid line) and transmission (dashed line) as a function of the focal distance of OE1.

the diffraction by the finite OE size. The relative flux density is higher and increases faster than the 1:1 FO demagnification case as the BDA size increases.

In general, a larger FO demagnification ratio provides smaller beam size but lower flux. Based on the requirement of the experiment, one can optimize the beamline design by choosing the appropriate FO demagnification, or the BDA position. One should also note that a large FO demagnification design will require the accurate control of the BDA size down to one micron level, which is an engineering challenge.

The major advantage of case 3 over case 1 is that the BDA isolates the vibration effects from the source, the monochromator, and other upstream optics. Once the FO demagnification factor is determined, the two mirror length of OE can be optimized similarly as shown in Fig. 3 for case 1.

4. ZOOM OPTICS

Many APS-U beamlines have been demanding variable focal spot sizes over a large range of values to adapt to different sample sizes while maintaining the same focus position. In general, this “zoom optics” arrangement can be achieved (in each orthogonal direction) by using two focusing elements at different distances upstream of the sample. The optics can be either transmission optics (e.g., CRLs) or reflective optics (e.g., mirrors) or a combination of the two. For the APS-U, four beamlines are under design with the CRL or/and mirror based zoom system. The zoom capability of the system depends on the focusing condition and positions of the two optics.

Fig. 5 shows the three zoom geometries and the calculated horizontal focal spot size and transmission as a function of the focal distance of the first focusing optics (OE1). In this calculation, the source is the same as in Section 3; OE1 located at 50 m from the source is a 400 mm long mirror that takes the full horizontal beam; and OE2 located at 69.8 m from the source is a 200 mm long mirror; the working distance between the downstream end of OE2 and the sample is 100 mm. Both mirrors have a grazing angle of 4 mrad with a reflectivity of 90%. The zoom geometry 2 is the most common setup using deformable mirrors because that it can provide a large range of spot sizes. The creation of a real secondary source is also beneficial for cleaning the beam with slits.²⁷ The zoom geometry 3 is normally used with CRLs. By changing the number of lenses in the two sets of CRLs, discrete focal spot sizes can be achieved. In this case, using OE1 (CRL1) alone to focus directly gives the largest focal spot size, while using OE2 (CRL2) alone gives the smallest focal spot size. The zoom geometry 1 is less common but accessible if convex lenses or mirrors are used.

In this section, we take one of the APS-U feature beamlines, ATOMIC, as an example to discuss the design of a KB mirror-based zoom optics using the concept that was demonstrated previously.^{28,29} Fig. 6 shows the

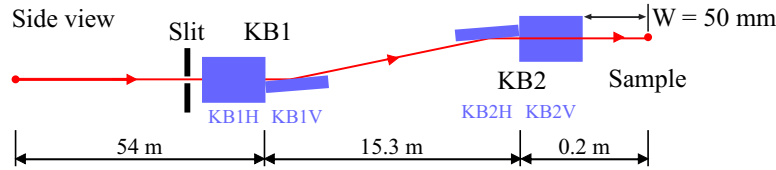


Figure 6. Schematic of the zoom KB system for the ATOMIC beamline.

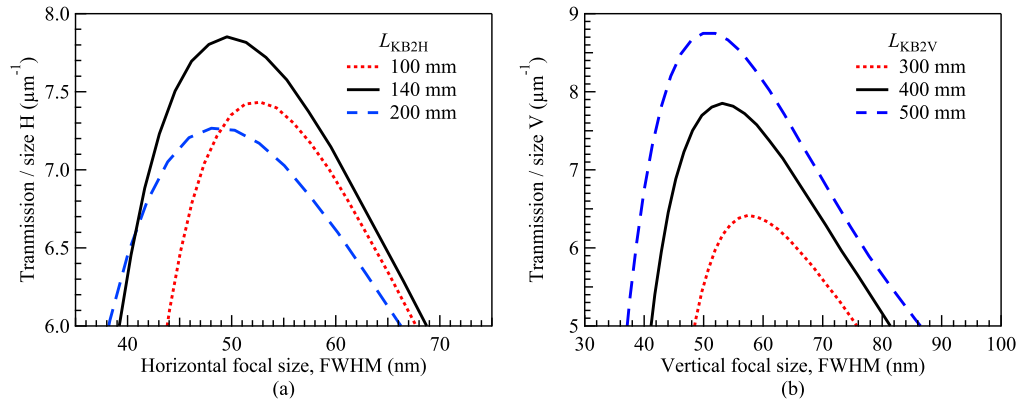


Figure 7. Calculated flux density at the focal plane of the zoom KB system as a function of the focal size with different lengths of (a) KB2H and (b) KB2V.

schematic of the zoom KB system for the ATOMIC beamline. The designed focusing range is 50 nm to 1.5 μm . The source is a 2.1 m long undulator with a position offset of $\delta_u = 1.25$ m from the center of the straight section. The beam waist is assumed to be at $d_w = 1.07$ m, and it is assumed to be Gaussian with a RMS size of 15×5.0 μm^2 (H \times V) and a RMS divergence of 6.2×5.6 μrad^2 (H \times V). The first KB pair (KB1) and the second KB pair (KB2) are located at 54 m and 69.3 m from the center of the straight section, respectively. All four mirrors are having a grazing angle of 3 mrad. There is a 10 mm separation between the edges of the two mirrors in each KB pair. The slit before KB1 used in this example is open to one coherent length in each direction as defined by Eq. 7. The length of the horizontal (KB1H) and vertical mirror (KB1V) of the KB1 pair is determined by the largest beam acceptance of the slit (lowest coherence acceptable by the experiment). Here we assume both KB1H and KB1V are 350 mm long. On the other hand, the length of the horizontal (KB2H) and vertical mirror (KB2V) of the KB2 pair is determined by optimizing the flux density for a 50 nm focus. Fig. 7(a) and (b) show the analytical calculation of the flux density as a function of the focal size with different KB2H and KB2V lengths, respectively. Increase the length of KB2H increases the total acceptance of the beam, but enlarges the focal spot size. To achieve the maximum flux density for a 50 nm focus, the optimum KB2H length is around 140 mm. On the other hand, increasing the KB2V mirror length up to 500 mm has a continuous increase in the flux density. Considering the manufacture challenges, the KB2V length will be mostly driven by the procurement. In the following simulation we use a KB2V length of 400 mm.

The figure error specification of these nano-focusing mirrors is the next essential step in the design process. It has been shown that the power spectrum density (PSD) function of the mirror figure profile is needed to simulate the effects on the focused beam.¹² Here we use the KB2V mirror as an example. The error profile of an elliptical cylinder (dabam-020 from the DABAM database,¹³ measured at Helmholtz-Zentrum Berlin) was scaled to the length of KB2V [cf. Fig. 8(a)]. *SHADOW-HYBRID* was used to calculate the effects of figure errors on the focused beam. The KB1V mirror was assumed to be a perfect elliptical cylinder focusing the source to a secondary source at 3.5 m downstream of KB1V. The KB2V mirror parameters are set to focus the secondary source to the image plane at 400 mm downstream from the center of KB2V. Fig. 8(b) shows the simulated vertical beam profiles at the focal plane with the figure error profile in Fig. 8(a) scaled to different RMS height errors. The FWHM size for the case with no slope errors [the bottom curve in Fig. 8(b)] is 46 nm, slightly less than the analytical calculations. Since the figure errors give rise to additional structures in the profile, FWHM

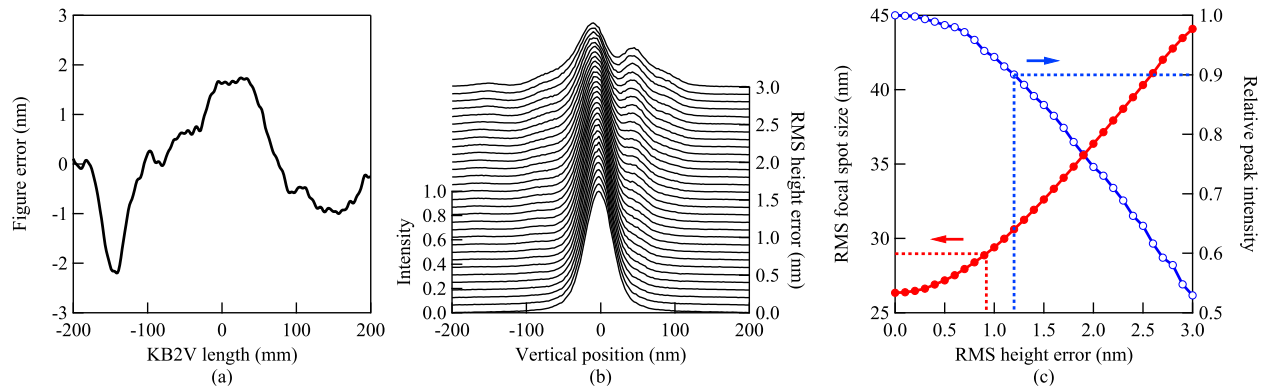


Figure 8. (a) The mirror figure error profile scaled from the dabam-020 mirror in the DABAM database¹³ with an RMS height error of 1 nm. (b) *SHADOW-HYBRID* simulations of the vertical beam profiles at the focal plane with the figure error profile in (a) scaled to different RMS height errors. (c) RMS focal spot sizes within the (-100 nm, 100 nm) range (solid circles) and relative peak intensities (open circles) of the focal beam as a function of the RMS height error extracted from (b). The dotted and dashed lines indicate the 10% increase in focal spot size and the 10% loss in peak intensity, respectively.

is not a good measure of the beam quality. Instead, the RMS size within the (-100 nm, 100 nm) range and the relative peak intensity of the focused beam were extracted from Fig. 8(b) and presented in Fig. 8(c). From Fig. 8(c) one concludes that the RMS height error needs to be less than 0.9 nm to ensure that the focal spot size broadening and the peak intensity reduction are both less than 10%. One should note that, once the figure error on KB1V is also considered, the specification of KB2V will need to be studied accordingly. Otherwise cleanup slits can be installed.²⁷

Finally, the full mutual coherence function can be simulated with more advanced codes, e.g., the MOI model.^{18,19} The source MOI, $J(y_1, y_2)$, in the y direction is simplified by using the Gaussian Schell Model (GSM),³⁰ given by

$$J(y_1, y_2) = I_0 \sqrt{\exp\left(-\frac{y_1^2 + y_2^2}{2\sigma_y^2}\right)} \exp\left[-\frac{(y_1 - y_2)^2}{2\xi_y^2}\right], \quad (12)$$

where I_0 is the maximum intensity, y_1 and y_2 are the coordinates at the source plane, and σ_y and ξ_y are the source size and transverse coherence length, respectively. The MOI source with parameters $\sigma_y = 5.0 \mu\text{m}$ and $\xi_y = 3.7 \mu\text{m}$ along the vertical direction was propagated through KB1V and KB2V using the same parameters as in the *SHADOW-HYBRID* case for three cases: without figure errors on KB2V and assuming RMS height errors of 0.5 nm and 1.0 nm on this mirror

The lower part of Fig. 9(a) shows the simulated local degree of coherence between any two points along the vertical axis (y axis) and $x = 0$ (horizontal axis) at the image plane without figure errors on KB2V. The middle part in the figure shows a cut of the two dimensional results at $y_2 = 0$. The top figure shows the beam intensity along the vertical direction obtained from the MOI propagation. As seen in the figure, the beam is highly, but not fully, coherent. The local coherence function is almost symmetric for the perfect mirrors.

Figs. 9(b) and 9(c) include the figure errors which were scaled from the profiles in Fig. 8(a) to have a RMS height error of 0.5 nm and 1.0 nm. Clearly, the figure errors redistribute the local correlation at the image plane, though the global degree of coherence is not altered.¹⁹ As seen in the upper figure of Fig. 9(b) the additional structure in the intensity graph corresponds to the region where the local degree of coherence is mostly affected. The RMS figure error of 1.0 nm (see Fig. 9(c)) has a significant effect on the local degree of coherence over all the region where the beam has intensity.

5. DISCUSSIONS AND CONCLUSIONS

We have shown the different levels of optics simulation and their usage in the design and optimization of beam-lines. The simple analytical approach can provide lots of useful information very quickly, such as the optics

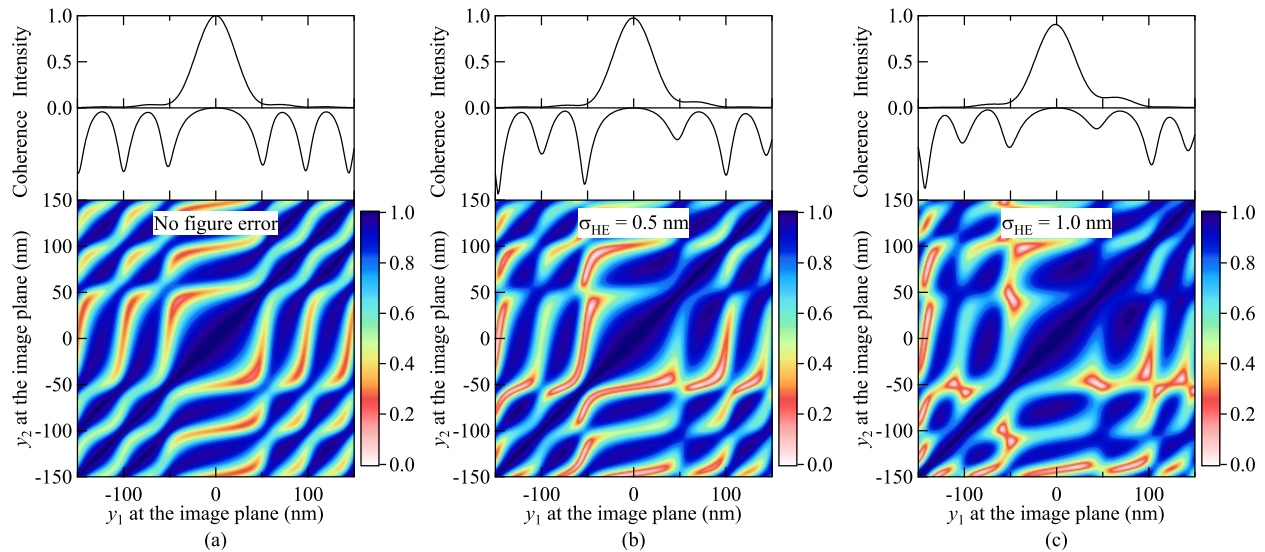


Figure 9. (Bottom figures) local degree of coherence between positions y_1 and y_2 , (middle figures) local degree of coherence between position y_1 and $y_2 = 0$, and (top figures) intensity profile in the vertical direction at the image plane calculated with the MOI model. The simulations were performed (a) without figure errors, (b) with 0.5 nm RMS height error, and (c) with 1.0 nm RMS height error on the KB2V mirror.

layout comparison, the optics position and size optimization, and the optics stability requirement. Ray-tracing and partially coherent beam propagation provides additional information for the expected beamline performance with non ideal optical elements and allows to determine the optics specification and mechanical requirements. There are general guidelines for selecting beamline layouts and optics. In this work, we show that the direct focusing geometry (case 1 in Fig. 1) and the secondary focusing geometry (case 3 in Fig. 1) are both compatible with the low-emittance storage rings. The case 3 is preferred to isolate vibrations of the upstream elements and to achieve small focal spots. Of course, the beamline design also needs to be optimized individually to accommodate requirements from various of X-ray techniques.

The zoom optics is a new concept that many beamlines are considering because of the broad range of sample environments and size scales. The initial choice of parameters is done with the analytical method, the design is confirmed and tested with *SHADOW-HYBRID* where the effect of figure errors is investigated. Finally the effect of figure errors on the local degree of coherence is investigated using the newly developed MOI model. The MOI model is currently under development to include real undulator sources and its extension to full two-dimensional calculation incorporating non-ideal optics.

This work is one of the steps towards the goal of performing simulations with the MOI model (or another development) that should allow to specify the required mirror quality that will fulfill the experimental needs on the local coherence.

Apart from the design challenge, the development of the zoom optics system also requires R&D on adaptive optics, which includes the manufacture of ultra-precision deformable mirrors, the in-situ optical metrology for monitoring the mirror surface profiles, the (non-invasive) wavefront sensor for measuring the beam shape, and the close-loop control system.

ACKNOWLEDGMENTS

This work was supported by the US Department of Energy, Office of Science, Office of Basic Energy Sciences, under Contract No. DE-AC02-06CH11357. The authors would like to thank Mr. Xiangyu Meng and Dr. Yong Wang from the Shanghai Synchrotron Radiation Facility for the useful discussion on the MOI calculation.

REFERENCES

- [1] Wolfram Research, Inc., “Mathematica 11.”
- [2] Cerrina, F., “Ray tracing of recent VUV monochromator designs,” *Proc. SPIE* **503**, 68–77 (1984).
- [3] Sanchez del Rio, M., Canestrari, N., Jiang, F., and Cerrina, F., “SHADOW3: a new version of the synchrotron X-ray optics modelling package,” *J. Synchrotron Rad.* **18**, 708–716 (2011).
- [4] Feldhaus, J., “RAY (unpublished),” (1984).
- [5] Schäfers, F., “The BESSY Raytrace Program RAY,” in [*Modern Developments in X-Ray and Neutron Optics*], Erko, A., Idir, M., Krist, T., and Michette, A. G., eds., ch. 2, 9–41, Springer-Verlag Berlin Heidelberg (2008).
- [6] Bergbäck Knudsen, E., Prodi, A., Baltser, J., Thomsen, M., Kjær Willendrup, P., Sanchez del Rio, M., Ferrero, C., Farhi, E., Haldrup, K., Vickery, A., Feidenhans'l, R., Mortensen, K., Meedom Nielsen, M., Friis Poulsen, H., Schmidt, S., and Lefmann, K., “McXtrace: A Monte Carlo software package for simulating X-ray optics, beamlines and experiments,” *J. Appl. Cryst.* **46**, 679–696 (2013).
- [7] Klementiev, K. and Chernikov, R., “Powerful scriptable ray tracing package xrt,” *Proc. SPIE* **9209**, 92090A (2014).
- [8] Shi, X., Reininger, R., Sanchez Del Rio, M., and Assoufid, L., “A hybrid method for X-ray optics simulation: combining geometric ray-tracing and wavefront propagation,” *J. Synchrotron Rad.* **21**, 669–678 (2014).
- [9] Shi, X., Sanchez Del Rio, M., and Reininger, R., “A new SHADOW update: integrating diffraction effects into ray tracing,” *Proc. SPIE* **9209**, 920911 (2014).
- [10] Rebuffi, L. and Sanchez del Rio, M., “ShadowOvi: a new visual environment for X-ray optics and synchrotron beamline simulations,” *J. Synchrotron Rad.* **23**, 1357–1367 (2016).
- [11] Sanchez del Rio, M., Rebuffi, L., Demsar, J., Canestrari, N., and Chubar, O., “A proposal for an open source graphical environment for simulating x-ray optics,” *Proc. SPIE* **9209**, 92090X (2014).
- [12] Shi, X., Assoufid, L., and Reininger, R., “How to specify super-smooth mirrors: simulation studies on nano-focusing and wavefront preserving x-ray mirrors for next-generation light sources,” *Proc. SPIE* **9687**, 968703 (2016).
- [13] Sanchez, M., Bianchi, D., Cocco, D., Glass, M., Metz, J., Raimondi, L., Rebuffi, L., Reininger, R., Shi, X., Siewert, F., Spielmann-jaeggi, S., Takacs, P., Tomasset, M., Vivo, A., and Yashchuk, V., “DABAM : an open-source database of x-ray mirrors metrology Contact author :,” *J. Synchrotron Rad.* **23**, 665–678 (2016).
- [14] Chubar, O., Berman, L., Chu, Y. S., Fluerasu, A., Hulbert, S., Idir, M., Kaznatcheev, K., Shapiro, D., Shen, Q., and Baltser, J., “Development of Partially-Coherent Wavefront Propagation Simulation Methods for 3rd and 4th Generation Synchrotron Radiation Sources,” *Proc. SPIE* **8141**, 814107 (2011).
- [15] Canestrari, N., Chubar, O., and Reininger, R., “Partially coherent X-ray wavefront propagation simulations including grazing-incidence focusing optics,” *J. Synchrotron Rad.* **21**, 1110–1121 (2014).
- [16] Singer, A. and Vartanyants, I. A., “Modelling of partially coherent radiation based on the coherent mode decomposition,” *Proc. SPIE* **8141**, 814106 (2011).
- [17] Glass, M., “Coherent modes for synchrotron light (comsyl),” <https://www.github.com/markglass/comsyl>.
- [18] Meng, X., Xue, C., Yu, H., Wang, Y., Wu, Y., and Tai, R., “Numerical analysis of partially coherent radiation at soft x-ray beamline,” *Opt. Express* **23**, 29675 (2015).
- [19] Meng, X., Shi, X., Wang, Y., Reininger, R., Assoufid, L., and Tai, R., “Mutual optical intensity propagation through non-ideal optics,” *J. Synchrotron Rad.* **24** (2017, accepted).
- [20] Elleaume, P., “Undulator radiation,” in [*Undulators, Wiggles and Their Applications*], Onuki, H. and Elleaume, P., eds., ch. 3, 69–107, CRC Press (2002).
- [21] Tanaka, T. and Kitamura, H., “SPECTRA: A synchrotron radiation calculation code,” *J. Synchrotron Rad.* **8**, 1221–1228 (2001).
- [22] Tanaka, T. and Kitamura, H., “Universal function for the brilliance of undulator radiation considering the energy spread effect,” *J. Synchrotron Rad.* **16**, 380–386 (2009).
- [23] van Cittert, P., “Die Wahrscheinliche Schwingungsverteilung in Einer von Einer Lichtquelle Direkt Oder Mittels Einer Linse Beleuchteten Ebene,” *Physica* **1**, 201–210 (1934).

- [24] Névot, L. and Croce, P., “Caractérisation des surfaces par réflexion rasante de rayons X. Application à l’étude du polissage de quelques verres silicates,” *Rev. Phys. Appl.* **15**, 761–779 (1980).
- [25] Borland, M., Sun, Y., Sajaev, V., Lindberg, R. R., and Berenc, T., “Lower emittance lattice for the advanced photon source upgrade using reverse bending magnets,” *Proc. of North American Particle Accelerator Conference (NAPAC’16)*, 877–880 (2016).
- [26] Kristiansen, P., Johansson, U., Ursby, T., and Jensen, B. N., “Vibrational stability of a cryocooled horizontal double-crystal monochromator,” *J. Synchrotron Rad.* **23**, 1076–1081 (2016).
- [27] Khakurel, K. P., Kimura, T., Nakamori, H., Goto, T., Matsuyama, S., Sasaki, T., Takei, M., Kohmura, Y., Ishikawa, T., Yamauchi, K., and Nishino, Y., “Generation of apodized X-ray illumination and its application to scanning and diffraction microscopy,” *J. Synchrotron Rad.* **24**, 142–149 (2017).
- [28] Kimura, T., Matsuyama, S., Yamauchi, K., and Nishino, Y., “Coherent x-ray zoom condenser lens for diffractive and scanning microscopy,” *Opt. Express* **21**, 9267 (2013).
- [29] Matsuyama, S., Nakamori, H., Goto, T., Kimura, T., Khakurel, K. P., Kohmura, Y., Sano, Y., Yabashi, M., Ishikawa, T., Nishino, Y., and Yamauchi, K., “Nearly diffraction-limited X-ray focusing with variable-numerical-aperture focusing optical system based on four deformable mirrors,” *Sci. Rep.* **6**, 24801 (2016).
- [30] Vartanyants, I. A. and Singer, A., “Coherence properties of hard x-ray synchrotron sources and x-ray free-electron lasers,” *New J. Phys.* **12**, 035004 (2010).